Japanese Journal of Applied Physics
Vol. 46, No. 4A, 2007, pp. 1392–1397

©2007 The Japan Society of Applied Physics

High-Performance Film Bulk Acoustic Wave Pressure and Temperature Sensors

Kuan-Hsun CHIU[1*], Hong-Ren CHEN[2], and Star Ruey-Shing HUANG[1,2]

[1]*Institute of Electronics Engineering, National Tsing Hua University, 101, Section 2, Kuang Fu Road, Hsinchu, Taiwan 300, R.O.C*
[2]*Asia Pacific Microsystems Inc., No.2 R&D Rd. VI, Science-based Industrial Park, Hsinchu, Taiwan 300, R.O.C*

(Received November 10, 2006; accepted December 14, 2006; published online April 5, 2007)

A film bulk acoustic wave resonator (FBAR)-based sensor for the simultaneous measurement of temperature and pressure with high sensitivity is fabricated and characterized. Temperature or pressure sensing is determined by the change in the series resonant frequency of the FBAR device when exposed to a measurement environment. For temperature sensing, measurement results show a sensitivity of 25.02 ppm/°C, a nonlinearity less than ±0.005% over the measurement range of 10 to 80 °C, and a hysteresis within ±0.005% in one temperature cycle. In pressure sensing, measured results show a sensitivity of 336.2 ppm/bar, a nonlinearity less than ±0.004% over the measurement pressure range of 0 to 2.07 bar, and a hysteresis within ±0.007% in one pressure cycle. [DOI: 10.1143/JJAP.46.1392]

KEYWORDS: FBAR, temperature sensor, pressure sensor

1. Introduction

Acoustic wave devices have been used in various commercial applications, among which the application of acoustic wave devices such as surface acoustic wave devices (SAW) and film bulk acoustic wave resonator (FBAR) devices in personal communication devices is rapidly growing. The use of acoustic wave devices in sensing applications is also increasing because as sensing devices they have higher sensitivity and reliability than other types of sensors. Mass sensors, temperature sensors, gas sensors, chemical sensors, humidity sensors, pressure sensors and bio sensors utilizing acoustic wave devices have been reported.[1–4)]

The use of acoustic wave resonators as both pressure and temperature sensors is very attractive due to their intrinsic high sensitivity and output being in the form of frequency, which is readily transformed to digital without the need for an analog-to-digital converter. In addition, they can also be designed to operate in frequency bands used in wireless communication. For example, wireless readout can be achieved using an oscillator circuit, which incorporates an acoustic resonator in the feedback loop of the oscillator; this oscillator circuit generates an electrical signal at the resonator resonance frequency.[5)] Moreover, acoustic wave sensors are also robust despite their extremely small size and light weight, that make them very suitable in automotive applications. A sensor with multiple sensing functions also has advantages in term of device size and cost over all other sensors put together. Although much work have been carried out on acoustic-wave-based multiple function sensors,[2,6,7)] to the best of our knowledge, there is as yet no work on sensors that simultaneously sense both pressure and temperature utilizing FBAR devices. In this paper, we report a pressure and temperature multifunction sensor based on membrane-type FBAR devices. The design and fabrication processes of the device are briefly described, and the sensitivity, linearity, and hysteresis of the sensor's performance are determined in the pressure range of 0 to 2.07 bar and the temperature range of 10 to 80 °C.

2. FBAR-Based Sensor Design

In thickness field excitation (TFE), the excitation field is perpendicular to the thickness of the film. A membrane-type FBAR is shown in Fig. 1. The FBAR consists of an aluminum nitride (AlN) piezoelectric film, which is sandwiched between two electrodes. The piezoelectric film transforms electrical energy into mechanical energy and *vice versa*. The TFE FBAR uses a thickness-oriented electric field, which is applied between two parallel plate electrodes, to generate a thickness-propagating longitudinal or compressive acoustic wave. Therefore, the fundamental resonant frequency of the FBAR is mainly determined by the properties of the piezoelectric film and can simply be expressed as

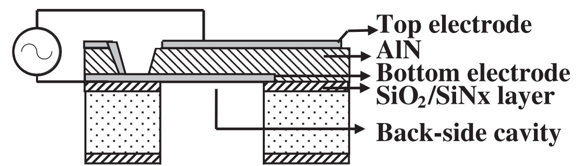

Fig. 1. Schematic plot of thickness field excitation membrane-type FBAR.

$$f = \frac{V_a}{2d}, \qquad (1)$$

where V_a is the phase velocity of the acoustic wave propagating in the piezoelectric film and d is the thickness of the piezoelectric film. The suspended FBAR having an air-surrounded membrane is so structured to prevent acoustic energy leaking out of the device; as the solid membrane and air boundary form a high impedance to acoustic waves, functioning as good acoustic wave reflectors. In addition, this suspended membrane structure facilitates FBAR bending deformation under pressure to achieve high sensitivity in pressure sensing, and also has high thermal resistance to reduce thermal energy loss through bulk solid conduction to achieve good temperature sensing.

According to eq. (1), the resonant frequency is determined by V_a and d, but in reality, the stimulated acoustic wave not only propagates in the piezoelectric film but also travels within metal electrodes. Hence, the effect of electrode materials must be taken into account.[8–10)] An accurate modeling of the TFE FBAR is performed using a one-dimensional Mason model that describes the electric characteristics of the piezoelectric film and an acoustic transmission line model that describes the nonpiezoelectic

*E-mail address: d899005@oz.nthu.edu.tw

electrode layers. The high-frequency performance of the FBAR can then be easily predicted using commercial software such as the advanced design system (ADS).

For simplicity in discussing the sensing behavior of the FBAR device, it is assumed that the electrodes are perfect wave propagation reflectors and that the attenuation in the piezoelectric film is negligible; thus the series resonant frequency (fs) of the FBAR, which is defined as the frequency at which minimum impedance is achieved, is mainly determined by the properties of the piezoelectric film, the excitation voltage V_a and the film thickness d.[11] According to acoustic physics, V_a can be expressed as

$$V_a = \sqrt{\frac{C}{\rho}}, \qquad (2)$$

where C and ρ are the stiffness matrix (or stiffness constant) and the mass density of the piezoelectric film, respectively.[9] C and ρ change when the film is subjected to mechanical stress and temperature change;[1,7] thus, V_a changes with a change in pressure or temperature. These changes in turn cause a shift in the fs of FBAR. This fundamental physical phenomenon is utilized in acoustic-wave-based sensors for pressure and temperature sensing.

3. Experimental Procedure

As described in the previous section, the AlN piezoelectric film serves as a key material, in which the transduction of electrical and mechanical energy takes place. Thus, a good AlN film is the key to improving the performance of the FBAR. In the desired AlN film crystallization, the (002) crystal orientation needs to be perpendicular to the bottom electrode surface. The crystal orientation of the reactive sputtered AlN film is strongly affected by many sputtering process parameters, such as sputtering power, sputtering pressure, N_2 concentration, substrate temperature and target-substrate distance.[12–15] Using the optimized parameters obtained from a systematic study of AlN deposition processing parameters, good (002)-oriented crystalline AlN films deposited by reactive sputtering, which exhibit exactly the same properties as a single crystal, were obtained. Figure 2 shows the X-ray diffraction (XRD) pattern and scanning electron microscopy (SEM) images of a good-quality AlN film for TFE FBAR fabrication. The XRD rocking curve pattern shown in Fig. 2(a) had a full width at half maximum (FWHM) of 2.7°, which confirms a preferential (002)-oriented AlN film. The hexagonal surface and column structure shown in Figs. 2(b) and 2(c), respectively, are also key features of the preferred (002)-oriented AlN film.

The fabrication process for the FBAR sensor is shown in Fig. 3, where processes can be divided into two stages: the fabrication of FBAR chips [Figs. 3(a) to 3(e)] and the package of the FBAR sensor [Fig. 3(f)]. The FBAR fabrication process is briefly described as follows. After the initial cleaning of a Si (100) wafer, a 1000-nm-thick SiO_2 layer was thermally grown and a 150-nm-thick SiN_x layer was deposited by plasma-enhanced chemical vapor deposition. A SiO_2/SiN_x stacked layer was used as the etching stop layer for inductive coupled plasma (ICP) backside silicon etching. Following the nitride deposition, a Pt/Ti (100/10 nm) film, the bottom electrode, was fabricated by a lift-off

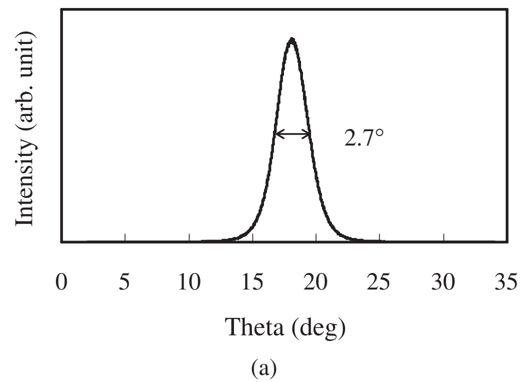

(a)

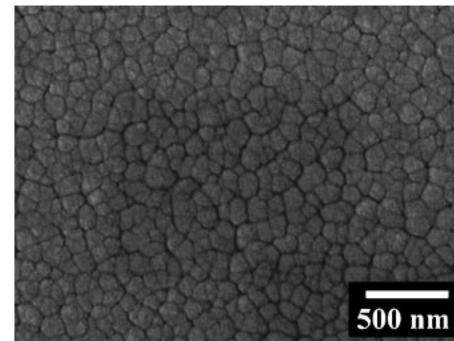

(b)

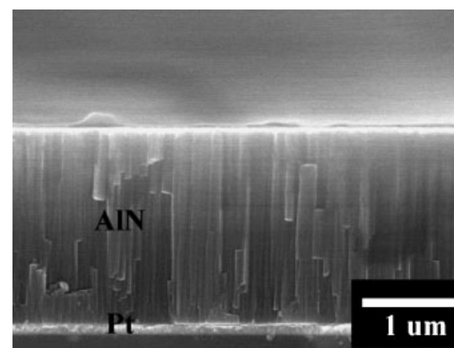

(c)

Fig. 2. (a) XRD rocking curve pattern, (b) plane-view SEM photograph and (c) cross-sectional SEM photograph of (002)-oriented AlN film.

process. The AlN film was then deposited by DC reactive sputtering to the desired thickness (about 2 µm). The AlN film was then lithographically patterned and etched with pure phosphoric acid (H_3PO_4) to open contact holes, which enable the access of electrical connection from bonding pads to the bottom electrode. The top aluminum electrode of 150 nm thickness was also fabricated by a lift-off process. Afterwards, the backside bulk silicon was etched into cavities by ICP to form membranes, which support the active areas of the devices. The SiO_2/SiN_x layer in the membrane region was then removed by reactive ion etching (RIE). Finally, the wafer was diced into individual FBAR chips.

To package an FBAR in a sensor for pressure and temperature sensing, an FBAR chip was mounted on a pre molded lead frame of a dual in-line package (DIP) with adhesive epoxy, and the backside cavity was aligned to the pressure inlet port to form a closed cavity, as shown in

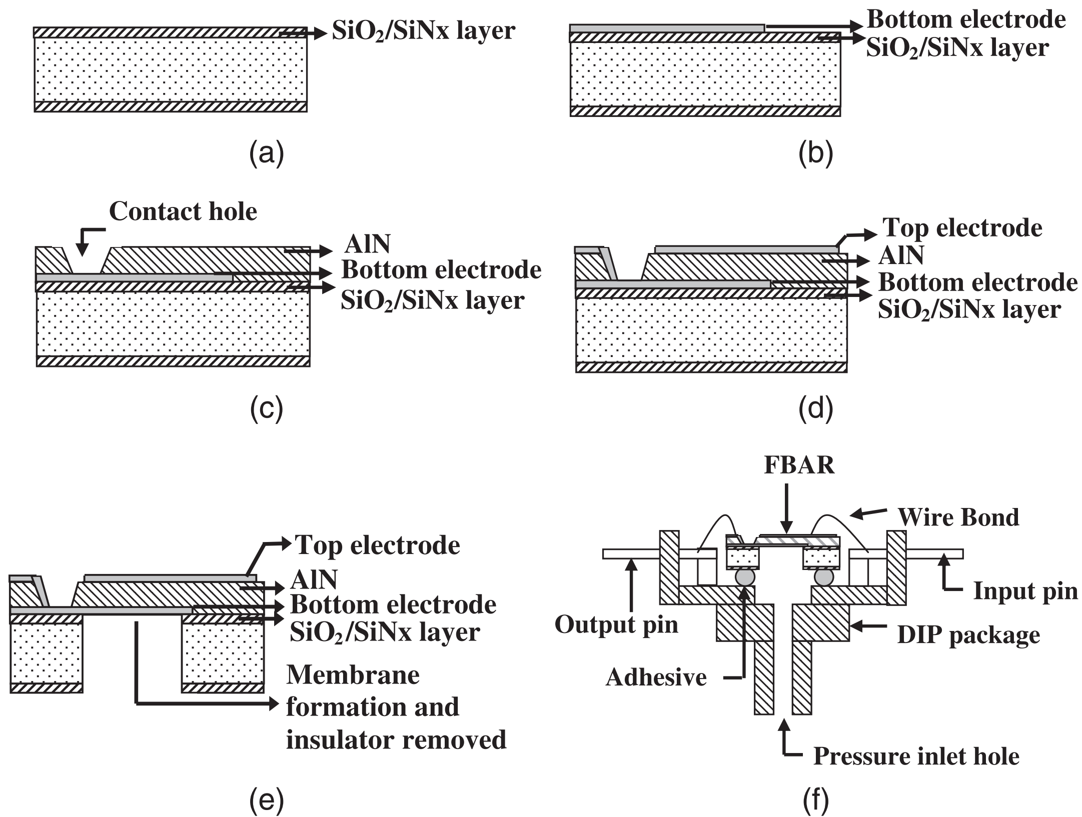

Fig. 3. Process flow of FBAR sensor. (a) Growth of SiO_2/SiN_x film; (b) deposition and patterning of Pt/Ti layer (bottom electrode); (c) deposition and patterning of AlN film; (d) deposition and patterning of Al film (top electrode); (e) membrane formation by ICP etching and insulator removal by RIE, and the wafer was dicing into individual FBAR chips. (f) Cross-section of FBAR sensor mounted on DIP package.

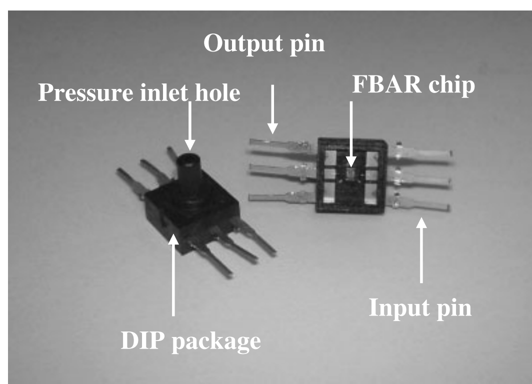

Fig. 4. Photograph of packaged FBAR-based sensor.

Fig. 3(f). Figure 4 shows a photograph of the packaged sensor. Pins of the DIP are configured to be compatible with a ground-signal-ground coplanar waveguide structure for high-frequency measurement with a network analyzer. After the FBAR was placed in the DIP, pins of the DIP were soldered to Sub Miniature version A (SMA) connectors. Then, the SMAs were connected to network analyzer inputs. The relationship of applied pressure and the FBAR's resonance frequency was measured and recorded by applying a hydrostatic pressure to the sensor via the inlet port from a calibrated pressure sensor test system, and temperature sensing was characterized in a calibrated temperature chamber.

4. Results and Discussion

In this study, we fabricated two FBAR-based sensors of different series resonant frequencies. Basically, these two FBAR-based sensors were fabricated using the process flow described in Fig. 3, except that the AlN film thicknesses of samples A and B were 2.27 and 2.15 μm, respectively. Figures 5(a) and 5(b) show the measured and simulation results of impedance characteristics for samples A and B at room temperature (20 °C) and atmospheric pressure, respectively. The solid lines represent the measured results and the dash lines represent the simulation results. The fs of the FBAR sensor was determined by the frequency at which the minimum is observed in the Z-parameter impedance characteristics. The series frequencies of samples A and B obtained were 1818.7 and 1897.2 MHz, respectively. The differences between the measured and simulation resonance frequencies were mainly due to the deposited thickness deviations from the designed values of the piezoelectric film. However, the measured series resonant frequencies of the FBAR sensors show a reasonably good agreement with the simulation results.

Figure 6(a) shows the temperature sensing of the FBAR sensor, specifically the series resonant frequencies vs temperature for FBAR sensors at atmospheric pressure. These two sensors characterized were designed to have different operating frequencies. The measured results show that, in both sensors, linear decreases in resonant frequency with increasing temperature were observed. We explain that the stiffness constant of the AlN film decreases as temper-

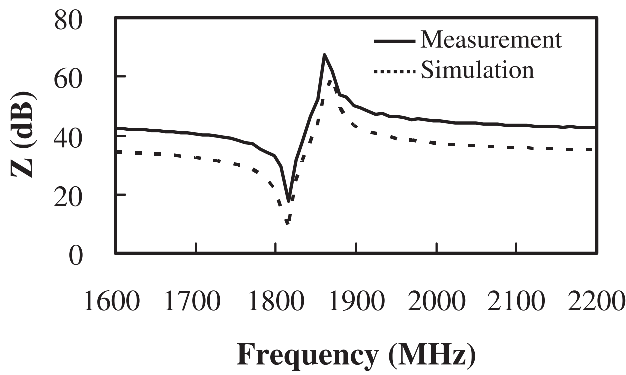

(a)

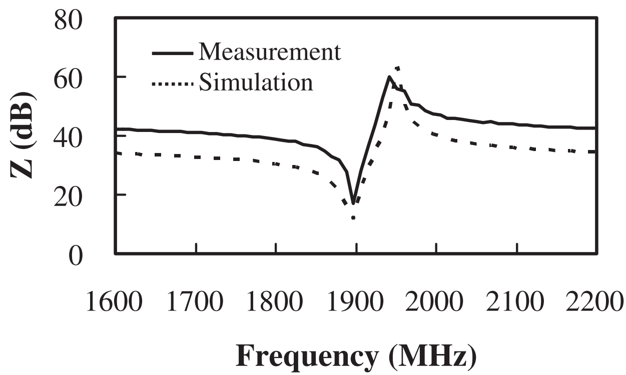

(b)

Fig. 5. Impedance characteristics of (a) sample A and (b) sample B. The solid and dash lines respresent the measured and simulation results, respectively.

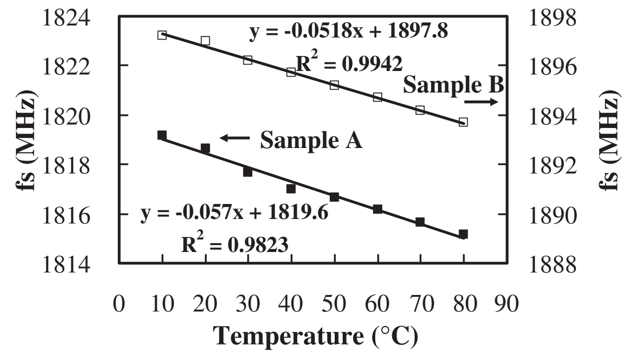

(a)

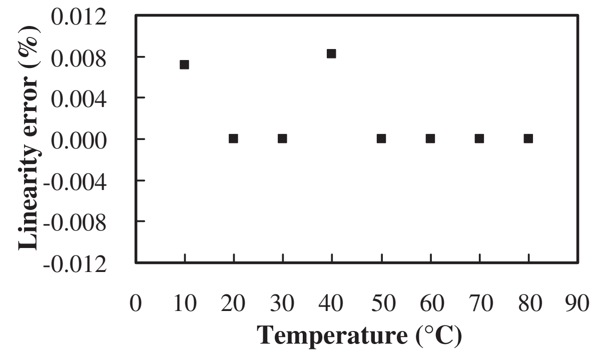

(b)

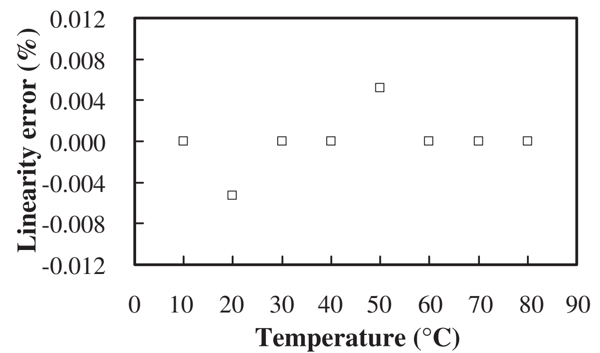

(c)

Fig. 6. (a) Resonant frequencies (fs) of FBAR sensors vs temperature measured at atmospheric pressure, (b) linearity error derived from least-squares best-fit straight line of sample A and (c) linearity error derived from least-squares best-fit straight line of sample B.

ature increases; consequently, resonant frequency decreases with increasing temperature. The fitted straight lines (by the linear least-squares method) show good linearity. As shown in Figs. 6(b) and 6(c), the calculated nonlinearities were within $\pm 0.008\%$ for sample A and within $\pm 0.005\%$ for sample B over the measurement temperature range. The sensitivity of the sensor was characterized by the ratio of the relative change in resonant frequency to a one-degree-centigrade change, and calculated to be 28.77 ppm/°C for sample A and 25.02 ppm/°C for sample B. The sensitivities of these two sensors were very close to the temperature coefficient of the AlN film,[16] because the AlN film was the key material of the FBAR sensor in the suspended structure.

Figure 7(a) shows the measured hysteresis of the temperature sensors between 10 to 80 °C. The solid line represents the series resonant frequency of the FBAR sensor when the temperature was increased from 10 to 80 °C and the dash line represents the measured resonant frequency when the temperature was decreased from 80 to 10 °C. Thermal hysteresis is the ratio of the difference in resonant frequency between the warmed up and the cooled down processes to resonant frequency. Figures 7(b) and 7(c) show the calculated thermal hysteresis for samples A and B, respectively. It is observed that the hystereses measured were within $\pm 0.009\%$ for sample A and within $\pm 0.005\%$ for sample B over the measurement temperature range. These measured results show that these sensors have good stability over the measurement temperature range and low hysteresis.

Figure 8(a) shows the pressure sensing results; the series resonant frequency vs applied pressure for FBAR sensors at room temperature was plotted. Note that the sensors exhibited different series resonant frequencies from those shown in Fig. 6(a); these differences are attributed to the fact that the DIP package introduces parasitics that are not de-embedded from the measurement results shown in Fig. 8(a). However, these differences do not affect sensor performance characterization because sensor performance is characterized by a relative change in series resonant frequency, not in the absolute value of resonant frequency. The measured results of pressure sensing shown in Fig. 8(a) demonstrate that the response in resonant frequency decreases linearly with increasing applied pressure for both sensors. These behaviors were explained to be caused by the phase velocity of the acoustic wave in the AlN film of FBAR being reduced when the FBAR is stressed under applied pressure. The

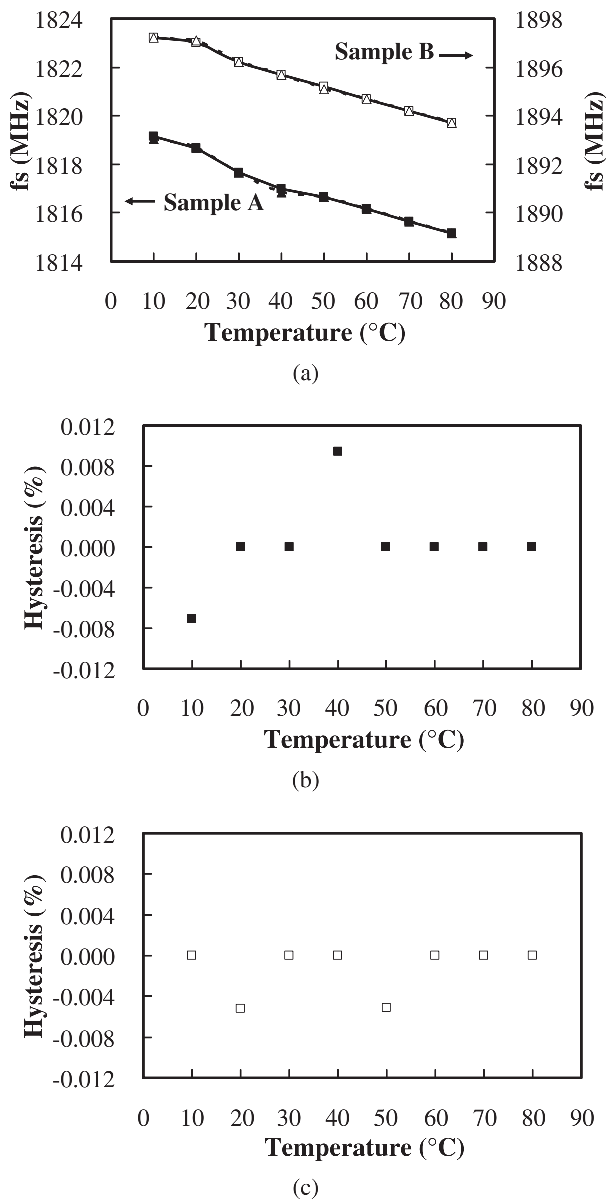

Fig. 7. (a) Thermal hysteresis study of FBAR sensors. The solid line represents measured results when the temperature was increased from 10 to 80 °C and the dash line represents measured results when the temperature was decreased from 80 to 10 °C. Calculated thermal hystereses of (b) sample A and (c) sample B.

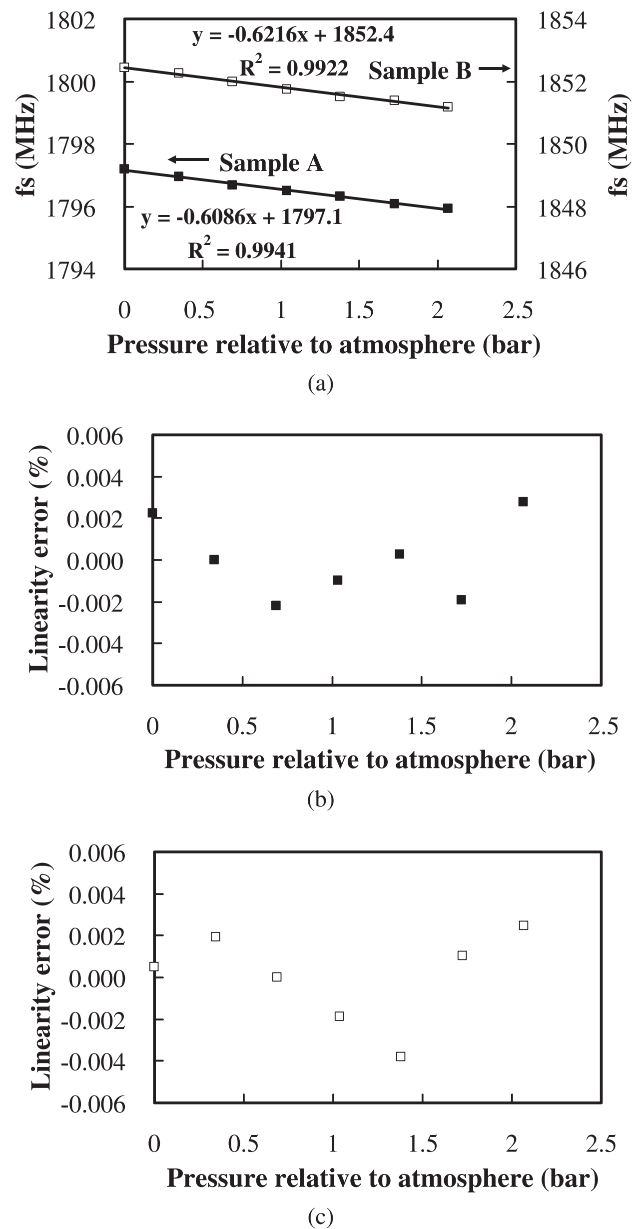

Fig. 8. (a) The resonant frequencies (fs) of FBAR sensors vs applied pressure measured at room temperature. (b) Linearity error derived from least-squares best-fit straight line of sample A. (c) Linearity error derived from the least-squares best-fit straight line of sample B.

nonlinearities calculated on the least-squares-fitted curve were within ±0.004% for sample A and within ±0.003% for sample B, respectively, over the measurement pressure range, as shown in Figs. 8(b) and 8(c). The sensitivity of the sensor was characterized by the ratio of the corresponding change in resonant frequency to a unit of pressure change, known as the gauge factor (*K*-factor) of a sensor, and calculated to be 336.2 (sensor A) and 309.9 (sensor B) ppm/bar. The sensitivities of these sensors were higher than those of other types of pressure sensor (typical *K*-factors of the resistor pressure sensor, piezoresistor pressure sensor, and SAW pressure sensor are 15, 100, and 200 ppm/bar, respectively).[3]

Figure 9(a) shows the hysteresis responses of the pressure sensors measured between 0 to 2.07 bar. The solid line represents the series resonant frequency of the FBAR sensor when pressure was increased from 0 to 2.07 bar, and the dash line represents the measured resonant frequency when the pressure was decreased from 2.07 to 0 bar. Pressure hysteresis is the ratio of the difference in resonant frequency between the increasing and decreasing pressure measurements to resonant frequency. Figures 9(b) and 9(c) show the calculated pressure hysteresis for samples A and B, respectively. These results show that the hystereses measured were within ±0.007% for sample A and within ±0.01% for sample B, respectively, over the entire measurement pressure range.

5. Conclusions

We have fabricated and characterized FBAR-based sensors for pressure and temperature sensing. These sensors were packaged in a form suitable for working in a non

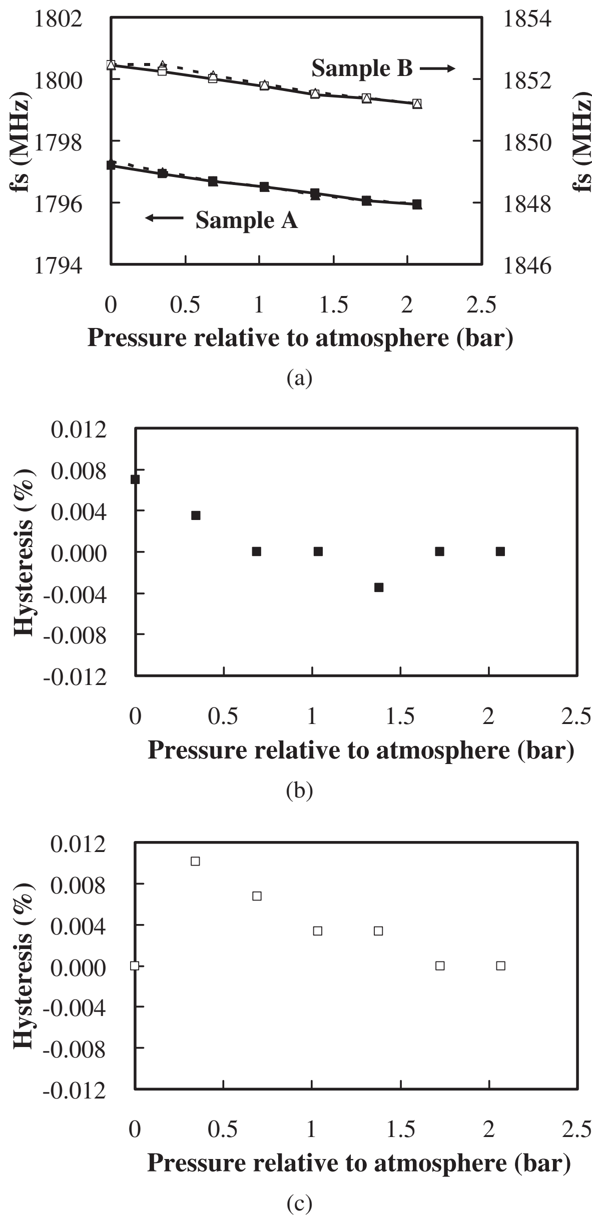

Fig. 9. (a) Pressure hysteresis study of FBAR sensors. The solid line represents measured results when pressure was increased from 0 to 2.07 bar and the dash line represents measured results when the pressure was decreased from 2.07 to 0 bar. Calculated pressure hystereses of (b) sample A and (c) sample B.

corrosive dry air ambient. The operating frequencies of these sensors were designed to be in 1800 MHz bands. The fabricated and characterized temperature sensor has a sensitivity of 28.77 ppm/°C in the temperature range from 10 to 80 °C, and the pressure sensor has a sensitivity of 336.2 ppm/bar over the pressure range from 0 to 2.07 bar. These sensors also show good linearity and low hysteresis over the measurement pressure and temperature ranges.

Acknowledgements

The authors would like to thank the support of the entire FBAR team of Asia Pacific Microsystems, Inc. for the device fabrication and measurement. The financial support for intern working experience for one of the authors, K. H. Chiu, is also appreciated.

1) H. Scherr, G. Scholl, F. Seifert, and R. Weigel: Proc. IEEE Ultrasonics Symp., 1996, p. 347.
2) R. Gabl, E. Green, M. Schreiter, H. D. Feucht, H. Zeininger, R. Primig, D. Pitzer, G. Eckstein, and W. Wersing: Proc. IEEE Sensors, 2003, p. 1184.
3) B. Jakoby, H. Eisenschmid, and F. Herrmann: IEEE Sens. J. **2** (2002) 443.
4) W. J. Fleming: IEEE Sens. J. **1** (2001) 296.
5) E. Benes, M. Groschl, F. Seifert, and A. Pohl: IEEE Trans. Ultrason. Ferroelectr. Freq. Control **45** (1998) 1314.
6) J. D. Sternhagen, C. E. Wold, W. A. Kempf, M. Karlgaard, K. D. Mitzner, R. D. Mileham, and D. W. Galipeau: IEEE Sens. J. **2** (2002) 301.
7) T. M. Reeder and D. E. Cullen: Proc. IEEE **64** (1976) 754.
8) K. M. Lakin: IEEE MTT-S Int. Microwave Symp. Dig., 1992, p. 149.
9) J. F. Rosenbaum: *Bulk Acoustic Wave Theory and Devices* (Artech House, Boston, 1988) pp. 371–449.
10) Q. X. Su, P. Kirby, E. Komuro, M. Imura, Q. Zhang, and R. Whatmore: IEEE Trans. Microwave Theory Tech. **49** (2001) 769.
11) A. E. Gerber and A. Ballato: *Precision Frequency Control-Oscillators and Standards* (Academic Press, Orlando, 1985) pp. 1–20.
12) C. C. Cheng, Y. C. Chen, H. J. Wang, and W. R. Chen: J. Vac. Sci. Technol. A **14** (1996) 2238.
13) H. Okano, Y. Takahashi, T. Tanaka, K. Shibata, and S. Nakano: Jpn. J. Appl. Phys. **31** (1992) 3446.
14) R. S. Naik, R. Reif, J. J. Lutsky, and C. G. Sodini: J. Electrochem. Soc. **146** (1999) 691.
15) K. H. Chiu, J. H. Chen, H. R. Chen, and R. S. Huang: Thin Solid Films **515** (2007) 4819.
16) K. M. Lakin: Proc. 45th Annual Symp. Frequency Control, 1991, p. 201.